

Geomorphological Analysis Using Unpiloted Aircraft Systems, Structure from Motion, and Deep Learning

Zhiang Chen, Tyler R. Scott, Sarah Bearman, Harish Anand,
Devin Keating, Chelsea Scott, J Ramón Arrowsmith, Jnaneshwar Das

Abstract— We present a pipeline for geomorphological analysis that uses structure from motion (SfM) and deep learning on close-range aerial imagery to estimate spatial distributions of rock traits (diameter, size, and orientation) along a tectonic fault scarp. Unpiloted aircraft systems (UAS) have enabled acquisition of high-resolution imagery at close range, revolutionizing domains such as infrastructure inspection, precision agriculture, and disaster response. Our pipeline leverages UAS-based imagery to help scientists gain a better understanding of tectonic surface processes. We start by using SfM on aerial imagery to produce georeferenced orthomosaics and digital elevation models (DEM), then a human expert annotates rocks on a set of image tiles sampled from the orthomosaics. These annotations are used to train a deep neural network to detect and segment individual rocks in the whole site. This pipeline automatically extracts semantic information (rock boundaries) on large volumes of unlabeled, high-resolution aerial imagery, which allows subsequent structural analysis and shape descriptors to result in estimates of rock diameter, size and orientation. We present results of two experiments conducted along a fault scarp in the Volcanic Tablelands near Bishop, California. We conducted the first experiment with a hexrotor and a multispectral camera to produce a DEM and five spectral orthomosaics in red, green, blue, red edge (RE), and near infrared (NIR). We then trained deep neural networks with different input channel combinations to study the most effective learning method for inference. In the second experiment, we deployed a DJI Phantom 4 Pro equipped with an RGB camera, and focused on the spatial difference of rock-trait histograms in a larger area. Although presented in the context of geology, our pipeline can be extended to a variety of geomorphological analysis tasks in other domains.

I. INTRODUCTION

Geographic Information Systems (GIS) have helped integrate a wide range of data sources, enabling efficient approaches for geological studies [1]. Traditionally, field surveys have been a gold standard for data collection because of low bias and high tolerance for dealing with ambiguity. However, field surveys are limited by access and time, and may not be as unbiased as previously assumed [2]. Meanwhile, remote sensing for collection of close-range terrestrial data has evolved from traditional methods such as airplanes, balloons, and kites equipped with cameras and LiDARs to the use of versatile robotic platforms such as Unpiloted Aerial Systems (UAS) or Unpiloted Aerial Vehicles (UAV). Combining data collection with UAS/UAV and Structure from Motion (UAS-SfM) offers a low-cost solution for rapid mapping of geologic sites, and generates

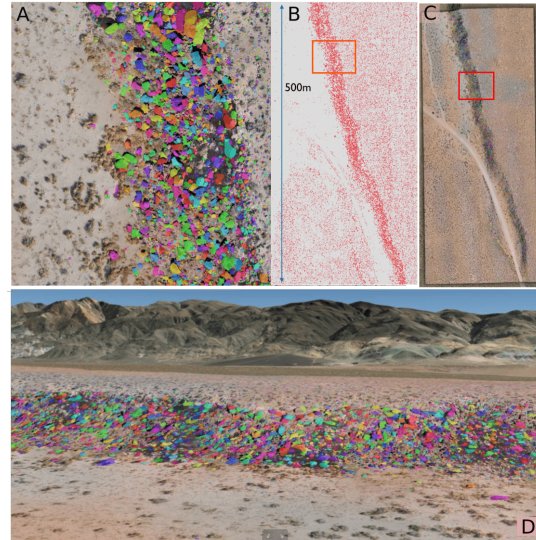


Fig. 1. Color segmentation visualization. (A) Partial enlargement of the red box in B and C. (B) Polygons of $\sim 80,000$ rocks from the site including outliers. (C) Segmentation on the area of study. (D) Ground view after loading the georeferenced Tiff image into Google Earth.

data products like digital surface models (DSM), digital elevation models (DEM), and cm-scale orthomosaics.

Our work is motivated by the need for precise, large spatial-scale estimation of geologic features. In this study, we collect and process data that potentially correlates with surface processes of tectonic fault scarps in Volcanic Tablelands near Bishop, California. Rock traits such as size, shape, orientation, and composition are of importance in earthquake geology research. Rock size distributions in the field site reflect both the initial cooling joint fracture geometry and the faulting-induced fracturing, which both vary with position as a function of strain magnitude and linkage characteristics. Rock orientations indicate the degree of downslope transport along the fault scarps, enhancing our understanding of erosional processes. Current analyses of topographical models produced by SfM largely rely on experts manually annotating features of interest (rocks).

In recent years, deep neural networks have demonstrated unprecedented success in image classification, segmentation, and object detection, leading to extensive application in satellite and airborne image analysis. Close-range UAS imagery provides higher-resolution features that extend the use of deep learning to rock trait estimation over a large range of rock sizes ranging as low as a few centimeters. Compared

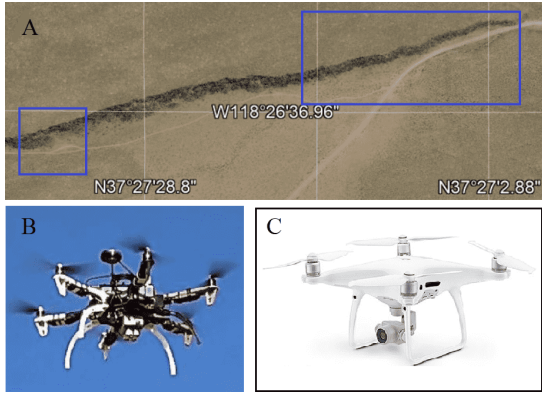


Fig. 2. Areas of study and UAVs. (A) Areas of study. The left-bottom rectangle: experiment 1; the right-top rectangle: experiment 2. (B) A hexrotor with a MicaSense RedEdge MX. (C) A DJI Phantom 4 Pro with an RGB camera.

to satellite based imaging, UAS imaging has the advantage of affordability, immediacy, agility, and sensor/camera flexibility.

We present a pipeline that combines UAS, SfM and deep learning (UAS-SfM-DL) to produce high-resolution semantic maps of objects, such as rocks, with wide variation in size and appearance (Fig. 3). We show that deep learning can be effectively applied on products from SfM, which may contain artifacts resulting from reconstruction. Advantages of the presented system include: low-cost, rapid deployment and analysis, statistically accurate results, high generalization to other fields, and automated processing with limited expert intervention. In comparison with deep learning methods on perspective UAS imagery [3], the UAS-SfM-DL paradigm can produce consistent georeferenced semantic maps, enabling large-scale, precise spatial analysis. Additionally, orthomosaics acquired through SfMs can potentially result in rich, high-resolution imagery of kilometer-scale sites. However, when applying deep neural networks on large orthomosaics, the model size increases significantly. Instead of relying on expensive computation, we propose an affordable solution that trains and infers on small tiles split from a large map. We present a registration algorithm to merge semantic objects from multiple tiles during inference.

We applied the UAS-SfM-DL system on two experiments analyzing rock traits along a tectonic fault scarp in Bishop, California (Fig. 2). In the first experiment, we equipped a hexrotor with a multispectral camera (MicaSense RedEdge MX) that can capture spectral imagery from five bands: R, G, B, RE, and NIR. The orthomosaics of the five channels and the DEM acquired from SfM were used to train a deep neural network to detect and segment individual rocks. We compared the neural network inference performance for different input channel combinations and discussed the influence of transfer learning for multi-channel inputs. In the second experiment, we deployed a DJI Phantom 4 Pro with an RGB camera and focused on the spatial difference of rock-trait histograms in a larger area. To our knowledge,

the UAS-SfM-DL system presents an unprecedented way to automatically characterize surface processes on fault scarps. Although presented in the context of geology, our pipeline can be extended to a variety of geomorphological analysis tasks in other domains such as crop property estimation in precision agriculture and debris field analysis after natural disasters.

II. RELATED WORK

A. Deep Learning in Close-range Aerial Imagery Processing

Deep learning has demonstrated unprecedented results in image classification [17], object detection [18], pixel segmentation [19], and instance segmentation [20]. The advances in computer vision have facilitated the development of visual perception models deployed aboard UAS as well as ground vehicles in various applications like wildfire classification [21], weed classification [4], car detection [3], and fruit counting [22]. However, previous work largely targets camera imagery as the input to the deep learning models. Although tracking algorithms [24] can reconstruct the objects of interest, they lack ground control points to globally correct geographic distortions, which is an essential step in geological and surveying applications. Deep learning has also been used to process 3D information, such as LiDAR point clouds. For example, point cloud data generated from scanning trees was fed to fully connected layers to classify tree types [25]. PointNet [26], designed to process point cloud data, was applied to classify urban objects [27]. 3D convolution neural networks have been used to segment point clouds from terrestrial laser scanning (TLS) [28].

B. Deep Learning in Satellite Based Remote Sensing

The deep learning research for satellite image processing has been one of the most active areas in remote sensing [30]. Applications of deep learning in remote sensing range from scene classification [32], object detection [34], and segmentation [35]. Apart from RGB images, deep learning has also been used on multi-spectral images [37]. Unsupervised learning plays an important role in feature learning from satellite images [38]. Super-resolution neural networks trained on available high-resolution ground truth have been used to enhance the resolution of satellite imagery [41]. However, resolution-enhanced satellite imagery cannot provide consistent and precise features needed for geological studies, as there may be artifacts from features learned on other sites. Additionally, due to image resolution (sub-meter to tens of meters per pixel), current deep learning research for satellite imagery analysis is limited to large-scale objects and features [43].

III. SYSTEM DESCRIPTION

The workflow of our UAS-SfM-DL pipeline is shown in Fig. 3. Although each individual component in the pipeline is not new, our focus is solving implementation issues and integrating them as a system in a practical case (rock instance segmentation) and other potential applications. Aerial imagery from UAS along with information of ground

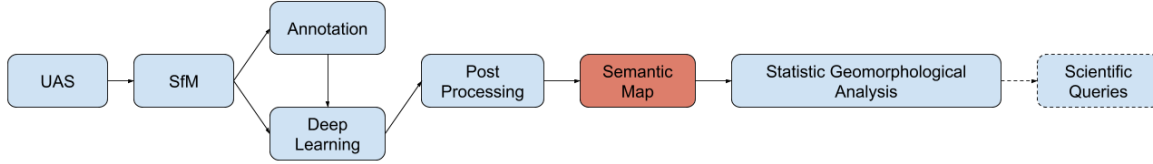


Fig. 3. Workflow of UAS-SfM-DL. The presented method expands the utility of the models from UAS-SfM.

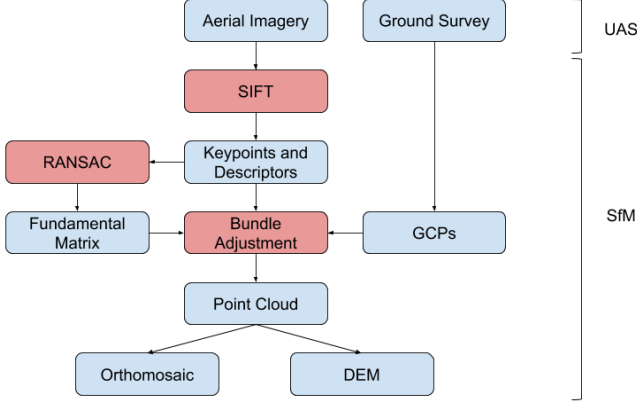


Fig. 4. UAS-SfM. Aerial imagery is taken from UAV surveys and then processed by SfM algorithms. GCPs are collected with precise GPS coordinate measuring equipment and provided to SfM algorithms to scale the 3D reconstruction and improve the mapping accuracy.

control points (GCPs) are processed using SfM algorithms to reconstruct a site of study with high-resolution. Geologists annotate features of interest, such as rock boundaries, for a portion of the high-resolution orthomosaic. Deep neural networks are trained on annotated images, and inference is carried out on unlabelled images from the whole site. Segmented objects inferred by the deep learning models are post-processed by geometric structural analysis and shape descriptors to estimate properties such as rock diameter and orientation. Semantic maps are produced by combining the semantic information from deep learning with post-processing. Statistics describing distribution of rock diameter and orientation are acquired from the resulting semantic maps, and they can provide a baseline for future geomorphological studies.

A. UAS-SfM

The framework of the UAS-SfM sub-system is shown in Fig. 4. With UAS imagery and GCPs, SfM based on bundle adjustment [triggs1999bundle] can produce precise georeferenced models like pointclouds, DEM, DSM, and orthomosaics for each spectral band. The orthomosaics and DEM are formatted as GeoTiff files with meta data information such as global coordinates, projection type, and ground resolution. These data allow us to acquire the global coordinates of each pixel in the map. The high-resolution orthomosaics enable precise spatial analysis of semantic features from deep learning.

B. Deep Learning

We use deep neural networks to automatically extract semantic information in large-scale georeferenced models produced from SfM. The advantage of using deep learning over manual feature engineering is that there is more flexibility in input data types. Deep learning accommodates complex inputs such as RGB orthomosaics, DEMs, and other spectral orthomosaics from multispectral cameras. The selection of neural network architecture depends on the features and distributions of objects of interest. We use the Mask-RCNN deep neural network architecture for this study because it generates both bounding boxes and the corresponding masks for object instances (rocks) [20]. Due to the densely-spatial distribution of rocks at this fault scarp, we select the Pyramid Feature Network (PFN) [46] as the backbone of the object detection network. PFN’s multi-scale, pyramidal hierarchy of anchor generation mechanism is suitable for object detection in such a setting. For other potential studies, segmentation neural networks such as U-Net [19] can be used when the goal is pixel-level segmentation. Region proposal networks such as Faster-RCNN [45] can detect individual objects with bounding boxes, though this information alone cannot produce geometric information of objects.

While it is common to scale spectral orthomosaics by intensity values, directly scaling DEM by elevation range values will overshadow the rock information in the scaled space. This is because the fault scarp slope elevation (20-30 meters) is greater than the height of most of the rocks (0.5-3 meters). To alleviate this issue, we use colormap (3 channels) to encode the DEM as shown in Fig. 5 (B). In doing so, we capture the absolute rock elevation in the colormap. However,

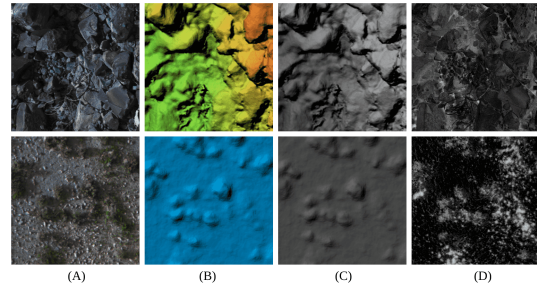


Fig. 5. DEM and spectral representations. (A) RGB tiles. (B) DEM colormap tiles. The color intensity indicates absolute elevation value above the ground surface on the lower side (hanging wall). (C) DEM grayscale tiles averaged from the r , g , b , of the DEM colormap: $p = 0.33r + 0.33g + 0.33b$. (D) Normalized difference vegetation index (NDVI).

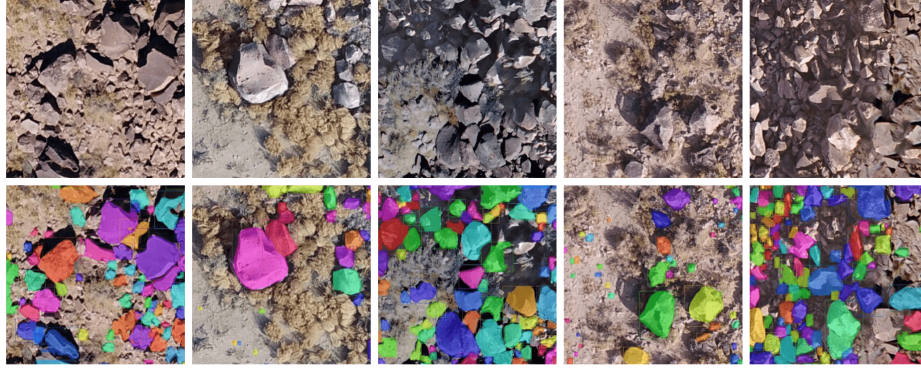


Fig. 6. Prediction of Mask RCNN on test dataset. Colors are randomly selected to distinguish rocks.

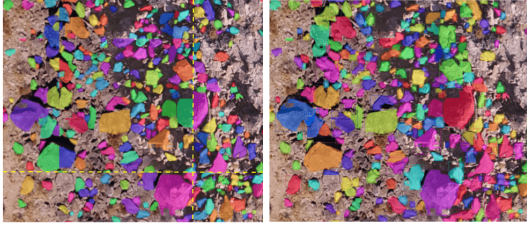


Fig. 7. Rock registration at boundaries. (Left) Rocks detected by the neural network at the edges of each inference are not merged; (right) any two rocks at the edges of each inference are merged and registered as one if they belong to same instance.

Algorithm 1 Rock Registration

input: orthomosaics, neural_network

output: registered_rocks

```

1. tiles = overlap_split(orthomosaics)
2. rocks = project(neural_network(tiles))
3. registered_rock = Empty_list
4. for rock in rocks:
    if rock.bbox is on its own tile edges:
        id = check_bbox_overlap(rock.bbox, registered_rocks)
        if id ≠ None:
            if check_IOU(rock.mask, registered_rocks[id].mask)
                > threshold:
                merge(registered_rocks[id], rock)
            continue
        register(registered_rocks, rock)

```

Comments:

overlap_split: splits orthomosaics into 400x400-pixel tiles with 10-pixel size overlap at four edges

project: projects local bounding boxes with pixel coordinates to global coordinates

check_bbox_overlap: returns None if there is no registered rocks having bounding box overlap with the rock, otherwise returns the overlapped registered rock's id

check_IOU: returns the intersection over union of two masks

merge: merges the bounding boxes and masks to the registered rock

register: registers new rock

only a local relative elevation representation is needed to assist rock instance segmentation, and it is unknown how the different representations may affect the neural network performance. Therefore, we introduce another DEM representation (Fig. 5 (C)) that averages the colormap from 3 channels, thus preserving the local relative elevation.

C. Tiling and Registration

The orthomosaics of survey sites produced by SfM are usually of high-resolution and large-scale (for our second fault scarp study, 2cm/pixel, 25664x10589). Directly working with high-resolution images for neural network training or inference is computationally challenging since it poses high demand on GPU RAM. To address this limitation, we split the orthomosaic into smaller tiles (400x400 pixels). We select a subset of tiles and annotate rocks using polygons in LabelMe [47], then divide them into a training dataset and a testing dataset. We augment the training dataset with a combination of random left-right flipping, top-down flipping, rotation, and zooming-in (cropping) and zooming-out.

When carrying out inference, we split the orthomosaics into 400x400 pixel tiles with 10-pixel overlap on four edges. Splitting the orthomosaics into tiles causes some rocks to be divided. As a result, rocks detected at the edges of tiles may belong to one single instance and risk getting treated as several smaller rocks as shown in Fig. 7 (right). To accommodate this problem, we apply a registration scheme to merge objects detected at the edges of tiles if they are from a single instance (Algorithm I). We determine that two georeferenced rock instances within the 10-pixel region of overlap are the same instance by checking if they share at least 20 pixels. If true, the two rock instances are merged and registered as one instance (Fig. 7 (left))

D. Post Processing

Post processing is necessary to compensate for errors that result from the data-driven nature of neural networks, and to identify the rocks on the fault scarp. The segmentation sub-network has stochastic errors, with one example shown in Fig. 9 (A) where a hole is present in the segmented rock body. We assume that there are no rocks with torus topology on the fault scarp, and use topological structure analysis to remove such artifacts [48]. The contours of rocks are generated, with the largest contours retained as the outlines of the rocks. The rock sizes are approximated by the number of pixels in the largest contours. Note that georeferenced models enable us to associate rock size in pixels and rock size

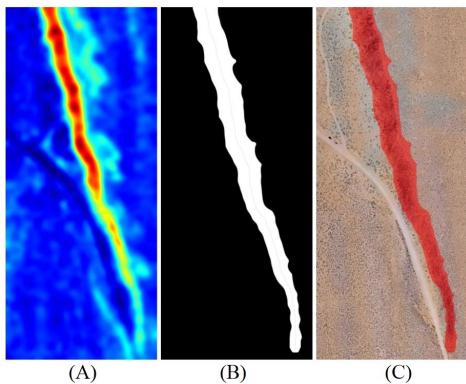


Fig. 8. Identifying the fault scarp. (A) Slope map. (B) Fault scarp contour. (C) Overlap with RGB orthomosaics.

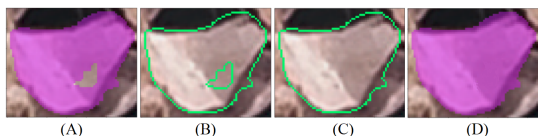


Fig. 9. Contour analysis to compensate for instability of segmentation prediction. (A) Mask prediction from Mask RCNN. (B) Contours by topological structure analysis. (C) The largest contour kept to approximate outline of the rock. (D) Filtered mask

in meters, which is more accurate than the association from perspective 2D camera photos whose scale is ambiguous.

Since the fault scarp has a steep slope, we first estimate gradient of the DEM [49], then denoise it with Gaussian filtering. From the smoothed slope map, the fault scarp is identified by the slope above a certain threshold and further smoothed through morphological transformations such as opening, dilation, erosion, and etc.

IV. EXPERIMENTS

In this section, we discuss the results of our pipeline in two experiments at the Volcanic Tablelands, which is a faulted plateau of approximately 150 meters thick welded Bishop Tuff (760 ka) at the north end of Owens Valley near Bishop, California.

A. Hexrotor and Multispectral Camera

The study area for this experiment is shown in the bottom left rectangle in Fig. 2 (A). We equipped a hexrotor with a RTK GPS and a straight-down multispectral camera (MicaSense RedEdge MX) that can capture spectral bands of blue (465-485 nm), green (550-570 nm), red (663-673 nm), red edge (712-722 nm), and near-IR (820-860 nm). The camera’s horizontal field of view is 47.2° . We deployed a lawn mower pattern with a flight altitude of 30-50 meters above ground level (the height of the fault scarp slope is about 20 meters). Agisoft Metashape [8] was used for SfM and produced five spectral orthomosaics and a DEM (9258x8694, 2cm/pixel). We split the spectral orthomosaics and DEM into 400x400 tiles with 10-pixel size overlap at four edges, and annotated

25 tiles for training and 5 tiles for testing. We augmented the training dataset 100 fold by the aforementioned method.

For the machine learning aspect of this experiment we are interested in two main questions: 1) Will additional input channels (RE, NIR, depth) improve a neural network’s performance? And 2) when the neural network has been pretrained with a benchmark dataset (e.g. COCO 2017), will transfer learning benefit the neural network if there are more input channels than just RGB? We inspected these two ideas by varying the input channel combinations and weight initialization as shown in Table I. To check the neural network inference performance we examined two datasets. The first dataset only contains the test data, and the second dataset contains all annotations (test + training datasets). We did this because we had a limited number of annotations and we wanted to avoid potential sampling bias. However, only examining training data does not indicate if the model is overfitting, therefore we examined the second dataset containing all annotations. Since this work is instance segmentation, our measures are average precision (AP) and average recall (AR) for both detection (bounding box) and segmentation (mask).

Results for Question 1: As shown in Table I, when the network is trained from scratch (no transfer learning) it generally performs better when additional information channels are included. However, we found that both detection and segmentation performance on the test dataset slightly declined when only depth information was added, with the exception of a few minor improvements in segmentation performance. For the combined dataset, detection and segmentation performance improved when any additional information was included, and we found that including all information resulted in the significant improvement for both datasets.

Results for Question 2: To answer our second question, we initialized our neural network with pretrained weights from COCO 2017. However, since COCO only contains RGB data, we initialized the first convolutional layer with weights from a Gaussian distribution for trials 6-8 in Table I to accommodate non-RGB inputs. When we compare inference performance in the test dataset with and without transfer learning, we find that transfer learning does not benefit the neural network inference prediction. We believe that our test dataset was too small and is inaccurate. However, when we compare the performance of the combined dataset with and without transfer learning, we find that only-RGB inputs significantly improve with transfer learning. When we compare the performance of the combined dataset within transfer learning, we find that additional channels generally

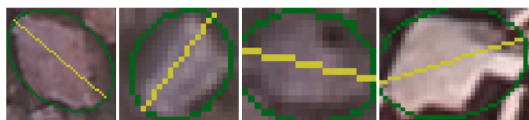


Fig. 10. Ellipse fitting and estimation of major orientations from the inferred rock boundaries. The yellow line shows the major axis.

TABLE I
EXPERIMENT 1: NEURAL NETWORK INFERENCE RESULT

			Test Dataset								All (Test Dataset + Training Dataset)							
			Detection (Bounding Box)				Segmentation (Mask)				Detection (Bounding Box)				Segmentation (Mask)			
			AP_1	AP_2	AP_3	AR	AP_1	AP_2	AP_3	AR	AP_1	AP_2	AP_3	AR	AP_1	AP_2	AP_3	AR
NTL	1	RGB	.252	.598	.217	.334	.222	.556	.133	.295	.216	.501	.152	.293	.185	.458	.124	.251
	2	RGB+DEM3	.250	.591	.150	.325	.224	.545	.140	.279	.254	.595	.168	.317	.225	.553	.141	.269
	3	RGB+DEM1	.250	.597	.137	.334	.226	.558	.136	.290	.251	.586	.164	.310	.226	.549	.137	.270
	4	RGB+RE+NIR+DEM3	.286	.617	.244	.386	.252	.573	.204	.346	.341	.712	.277	.400	.335	.708	.263	.387
TL	5	RGB	.251	.556	.184	.331	.224	.538	.129	.293	.350	.710	.295	.401	.342	.706	.237	.368
	6	RGB+DEM3	.240	.563	.155	.317	.220	.561	.154	.285	.241	.570	.166	.297	.225	.551	.148	.272
	7	RGB+DEM1	.250	.580	.166	.326	.214	.557	.118	.267	.284	.634	.205	.343	.285	.611	.141	.302
	8	RGB+RE+NIR+DEM3	.269	.613	.199	.356	.252	.591	.185	.329	.267	.611	.191	.340	.254	.596	.169	.319

* *NTL*: no transfer learning, *TL*: transfer learning, *IoU*: intersection over union, AP_1 : average precision for $IoU=0.5 : 0.95$, AP_2 : average precision for $IoU=0.5, AP_3$: average precision for $IoU=0.75$, AR : average recall for $IoU=0.5 : 0.95$, *DEM3*: DEM colormap, *DEM1*: DEM grayscale from DEM colormap

perform worse than only-RGB inputs. We see that adding depth information in the form of DEM1 improves performance with transfer learning, which we will explore in future work.

Only-RGB input with transfer learning is appealing because it has comparative performance by comparing trial 4 and 5, which achieve the top results in the combined dataset. Additionally considering the cost advantage of RGB cameras, we decided to only collect RGB data for Experiment 2.

B. DJI Phantom 4 Pro and RGB Camera

The goal of this experiment is to acquire rock trait information in a larger study area (Fig. 2) using RGB orthomosaics. We want to determine how rock trait histograms change along a fault scarp, and use this information as a baseline for future geomorphological analysis. We conducted surveys of the Volcanic Tablelands with a DJI Phantom 4 Pro, implementing a grid flight pattern with 66% image overlap, and a 90° (nadir) camera angle. The flight altitude varied between 70-100 meters above the ground level due to the height of the fault scarp slope (30 meters). The Megapixel onboard camera had an 84° field of view and 5472x3648 resolution, resulting in an effective spatial resolution of 3cm/pixel.

The 25664x10589 orthomosaics were split into 400x400 tiles. 51 tiles were annotated by human experts (45 tiles for training, and 6 for testing). The neural network was initialized with well trained weights from COCO 2017 and then retrained on one NVIDIA RTX 2080 Ti. We trained for 15 hours by stochastic gradient optimization with an initial learning rate 0.001, learning momentum 0.9, and weight decay 0.0001. The performance of the network is shown in Table II. Inference results on images from the test dataset are shown in Fig. 6.

To remove outliers on the perimeter, we identified the boundaries of the fault scarp from the slope map. The slope map and the fault scarp contour are shown in Fig. 8. The in-lying rocks were then estimated by the refined masks from topological structure analysis. The results of the filtered rock instances as color masks are shown in Fig. 1. Finally, we used the georeferenced rock boundary information to estimate rock diameter and orientation distribution. To approximate

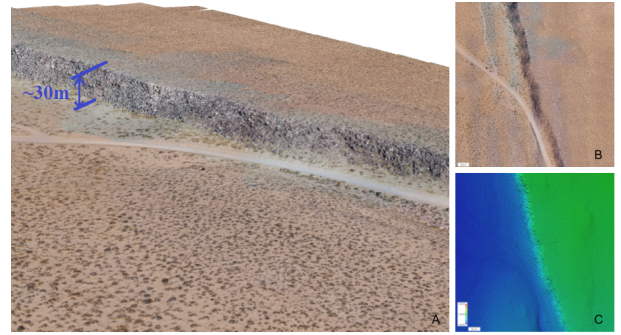


Fig. 11. Results of SfM. (A) A 3D point cloud; (B) RGB Orthomosaic; (C) DEM.

TABLE II
EXPERIMENT 2: NEURAL NETWORK INFERENCE RESULTS

	Detection (Bounding Box)				Segmentation (Mask)			
	AP_1	AP_2	AP_3	AR	AP_1	AP_2	AP_3	AR
Test	.350	.736	.303	.448	.316	.696	.242	.409
All	.280	.584	.227	.332	.282	.609	.218	.331

major orientations of rocks, we fitted the refined masks with ellipses as shown in Fig. 10. The orientations of rocks were parameterized by eccentricity and an angle describing the major axes of the ellipse. Fig. 12 (D) shows the polar histogram of major orientations.

We are not only interested in the distribution of rock traits along the length of the scarp, but along the cross strike as well, which is the perpendicular direction of the fault scarp (Fig. 13). We computed the skeleton of the fault scarp contour to acquire the middle spline [52], then selected a subsection of the spline and approximated it with a straight line by linear regression. We considered the normal vector of the straight line as the cross strike direction. The whole fault scarp is divided to 16 areas that are lying in the center of the spline. Each area is divided into 9 boxes along the cross strike direction. Within each box there are 20 bins representing the normalized rock diameter histogram in the true box. From the bottom (south) to top (north) in each area, the histogram axis (major-axis length) varies from 0 to 3.6 meters.

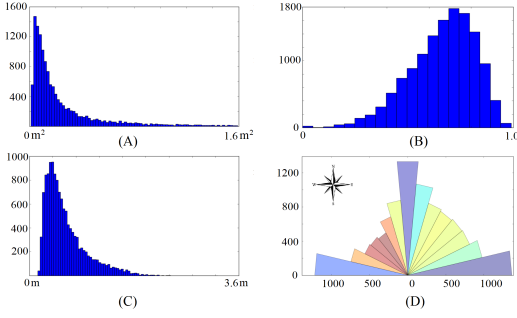


Fig. 12. Histograms of rock traits. (A) Rock size histogram on the fault scarp. The rock sizes are approximated by the area of the refined masks. The horizontal axis is rock area in $meters^2$, and the vertical axis is the number of rocks. (B) Rock eccentricity histogram on the fault scarp. (C) Rock major length histogram on the fault scarp. The major-axis length is $L = 2a$, where a is the semimajor axis of the fitting ellipse $\frac{x^2}{a^2} + \frac{y^2}{b^2} = 1$. (D) Polar histogram of major-axis orientation on the fault scarp.

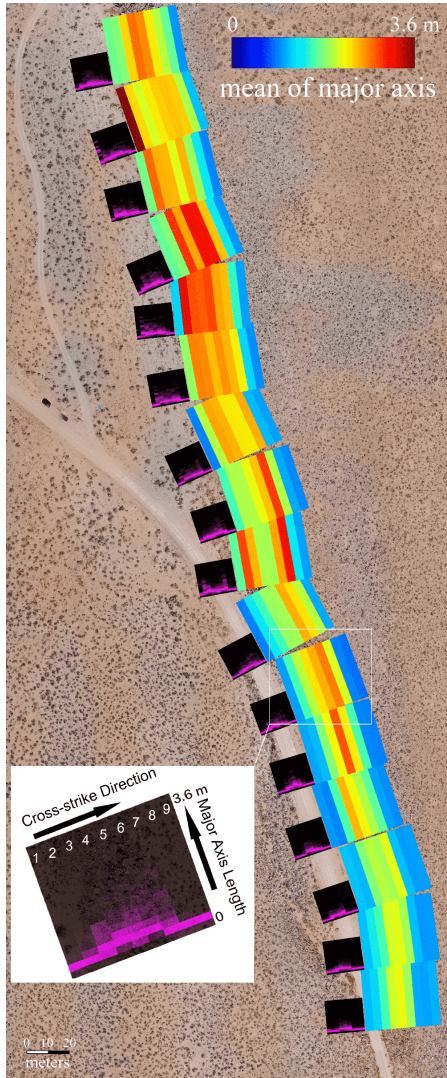


Fig. 13. Detailed rock diameter (major-axis length) colormap for the study area. The colormap on the fault scarp shows the mean rock diameter for each box along the scarp. The smaller black plots at the left show detailed histograms of rock diameter.

V. CONTRIBUTION AND FUTURE WORK

In this paper, we presented a pipeline for geomorphological analysis using structure from motion and deep learning on close-range aerial imagery. Our UAS-SfM-DL methodology was used to assess the effectiveness of including multispectral data in neural network training and to estimate distribution of rock traits (diameter and orientation) on a fault scarp in the Volcanic Tablelands, California. From our first experiment, we conclude that the neural network inference from RGB with transfer learning has comparative performance with RGB+RE+NIR+DEM (no transfer learning), which means this UAS-SfM-DL pipeline is scalable to commercial UAVs with color cameras.

From the second experiment, we focused on the spatial difference of the fault scarp in a larger area. As far as we know, this is the first time that UAVs and machine learning are used to obtain the histograms of rock traits on fault scarps. We can see from our figure that the distributions of rock size are asymmetrical throughout the fault, with larger rocks in the north and smaller rocks in the south. This information can guide future scientific inquiry about strain across the fault to better understand earthquakes in a tectonically active region.

We used Mask RCNN and only modified the first convolutional layer for different input channels. In doing so, the feature descriptors (convolutional filters) at low-level neural network were changed, which can be a reason that transfer learning did not improve performance when additional channels are input. We will investigate this problem and explore neural network architectures that can produce better neural network performance by both reusing pretrained weights and integrating additional channel inputs.

ACKNOWLEDGEMENTS

This work was supported in part by Southern California Earthquake Center (SCEC) award 19179, and National Science Foundation award CNS-1521617.

REFERENCES

- [1] Michael F Goodchild. “Twenty years of progress: GIScience in 2010”. In: *Journal of spatial information science* 2010.1 (2010), pp. 3–20.
- [2] J Barrett Salisbury et al. “Validation of meter-scale surface faulting offset measurements from high-resolution topographic data”. In: *Geosphere* 11.6 (2015), pp. 1884–1901.
- [3] Nassim Ammour et al. “Deep learning approach for car detection in UAV imagery”. In: *Remote Sensing* 9.4 (2017), p. 312.
- [4] Calvin Hung, Zhe Xu, and Salah Sukkarieh. “Feature learning based approach for weed classification using high resolution aerial images from a digital camera mounted on a UAV”. In: *Remote Sensing* 6.12 (2014), pp. 12037–12054.

- [5] Minas Spetsakis and John Yiannis Aloimonos. "A multi-frame approach to visual motion perception". In: *International Journal of Computer Vision* 6.3 (1991), pp. 245–255.
- [6] Carlo Tomasi and Takeo Kanade. "Shape and motion from image streams under orthography: a factorization method". In: *International Journal of Computer Vision* 9.2 (1992), pp. 137–154.
- [7] Noah Snavely et al. "Scene reconstruction and visualization from community photo collections". In: *Proceedings of the IEEE* 98.8 (2010), pp. 1370–1390.
- [8] Agisoft Photoscan. <https://www.agisoft.com/>. 2018.
- [9] Pix4D. <https://www.pix4d.com/>. 2019.
- [10] Matthew J Westoby et al. "'Structure-from-Motion' photogrammetry: A low-cost, effective tool for geoscience applications". In: *Geomorphology* 179 (2012), pp. 300–314.
- [11] MW Smith, JL Carrivick, and DJ Quincey. "Structure from motion photogrammetry in physical geography". In: *Progress in Physical Geography* 40.2 (2016), pp. 247–275.
- [12] Francesco Mancini et al. "Using unmanned aerial vehicles (UAV) for high-resolution reconstruction of topography: The structure from motion approach on coastal environments". In: *Remote Sensing* 5.12 (2013), pp. 6880–6898.
- [13] A Lucieer, Sharon A Robinson, and D Turner. "Unmanned aerial vehicle (UAV) remote sensing for hyperspatial terrain mapping of Antarctic moss beds based on structure from motion (SfM) point clouds". In: (2011).
- [14] Andrea Donnellan et al. "Geodetic Imaging of Fault Systems from Airborne Platforms: UAVSAR and Structure from Motion". In: *IGARSS 2018-2018 IEEE International Geoscience and Remote Sensing Symposium*. IEEE. 2018, pp. 7878–7881.
- [15] Kristen L Cook. "An evaluation of the effectiveness of low-cost UAVs and structure from motion for geomorphic change detection". In: *Geomorphology* 278 (2017), pp. 195–208.
- [16] MP Bunds et al. "Three Dimensional Aseismic Creep Deformation from Differencing of Structure from Motion and LiDAR High Resolution Topography on the San Andreas Fault, California". In: *AGU Fall Meeting Abstracts*. 2018.
- [17] Kaiming He et al. "Deep residual learning for image recognition". In: *Proceedings of the IEEE conference on computer vision and pattern recognition*. 2016, pp. 770–778.
- [18] Ross Girshick. "Fast r-cnn". In: *Proceedings of the IEEE international conference on computer vision*. 2015, pp. 1440–1448.
- [19] Olaf Ronneberger, Philipp Fischer, and Thomas Brox. "U-net: Convolutional networks for biomedical image segmentation". In: *International Conference on Medical image computing and computer-assisted intervention*. Springer. 2015, pp. 234–241.
- [20] Kaiming He et al. "Mask r-cnn". In: *Proceedings of the IEEE international conference on computer vision*. 2017, pp. 2961–2969.
- [21] Yi Zhao et al. "Saliency detection and deep learning-based wildfire identification in UAV imagery". In: *Sensors* 18.3 (2018), p. 712.
- [22] Steven W Chen et al. "Counting apples and oranges with deep learning: A data-driven approach". In: *IEEE Robotics and Automation Letters* 2.2 (2017), pp. 781–788.
- [23] Xu Liu et al. "Robust fruit counting: Combining deep learning, tracking, and structure from motion". In: *2018 IEEE/RSJ International Conference on Intelligent Robots and Systems (IROS)*. IEEE. 2018, pp. 1045–1052.
- [24] Xu Liu et al. "Monocular Camera Based Fruit Counting and Mapping with Semantic Data Association". In: *IEEE Robotics and Automation Letters* (2019).
- [25] Haiyan Guan et al. "Deep learning-based tree classification using mobile LiDAR data". In: *Remote Sensing Letters* 6.11 (2015), pp. 864–873.
- [26] Charles R Qi et al. "Pointnet: Deep learning on point sets for 3d classification and segmentation". In: *Proceedings of the IEEE Conference on Computer Vision and Pattern Recognition*. 2017, pp. 652–660.
- [27] Younes Zegaoui et al. "Urban object classification with 3D Deep-Learning". In: *JURSE: Joint Urban Remote Sensing Event*. 2019.
- [28] Zhou Guo and Chen-Chieh Feng. "Using multi-scale and hierarchical deep convolutional features for 3D semantic classification of TLS point clouds". In: *International Journal of Geographical Information Science* (2018), pp. 1–20.
- [29] Liangpei Zhang, Lefei Zhang, and Bo Du. "Deep learning for remote sensing data: A technical tutorial on the state of the art". In: *IEEE Geoscience and Remote Sensing Magazine* 4.2 (2016), pp. 22–40.
- [30] Xiao Xiang Zhu et al. "Deep learning in remote sensing: A comprehensive review and list of resources". In: *IEEE Geoscience and Remote Sensing Magazine* 5.4 (2017), pp. 8–36.
- [31] Qin Zou et al. "Deep learning based feature selection for remote sensing scene classification". In: *IEEE Geoscience and Remote Sensing Letters* 12.11 (2015), pp. 2321–2325.
- [32] Nataliia Kussul et al. "Deep learning classification of land cover and crop types using remote sensing data". In: *IEEE Geoscience and Remote Sensing Letters* 14.5 (2017), pp. 778–782.
- [33] Xueyun Chen et al. "Vehicle detection in satellite images by hybrid deep convolutional neural networks". In: *IEEE Geoscience and remote sensing letters* 11.10 (2014), pp. 1797–1801.
- [34] Tianwen Zhang and Xiaoling Zhang. "High-Speed Ship Detection in SAR Images Based on a Grid

- Convolutional Neural Network”. In: *Remote Sensing* 11.10 (2019), p. 1206.
- [35] Michael Kampffmeyer, Arnt-Borre Salberg, and Robert Jenssen. “Semantic segmentation of small objects and modeling of uncertainty in urban remote sensing images using deep convolutional neural networks”. In: *Proceedings of the IEEE conference on computer vision and pattern recognition workshops*. 2016, pp. 1–9.
- [36] Maria Vakalopoulou et al. “Building detection in very high resolution multispectral data with deep learning features”. In: *2015 IEEE International Geoscience and Remote Sensing Symposium (IGARSS)*. IEEE. 2015, pp. 1873–1876.
- [37] Hannah R Kerner et al. “Novelty Detection for Multispectral Images with Application to Planetary Exploration”. In: *Proceedings of the AAAI Conference on Artificial Intelligence*. Vol. 33. 2019, pp. 9484–9491.
- [38] Adriana Romero, Carlo Gatta, and Gustau Camps-Valls. “Unsupervised deep feature extraction for remote sensing image classification”. In: *IEEE Transactions on Geoscience and Remote Sensing* 54.3 (2015), pp. 1349–1362.
- [39] Qian Shi, Xiaoping Liu, and Xia Li. “Road detection from remote sensing images by generative adversarial networks”. In: *IEEE access* 6 (2018), pp. 25486–25494.
- [40] Kui Jiang et al. “Deep distillation recursive network for remote sensing imagery super-resolution”. In: *Remote Sensing* 10.11 (2018), p. 1700.
- [41] Jonathan Chin and Asif Mehmood. “Generative adversarial networks based super resolution of satellite aircraft imagery”. In: *Pattern Recognition and Tracking XXX*. Vol. 10995. International Society for Optics and Photonics. 2019, 109950W.
- [42] Ying Tai, Jian Yang, and Xiaoming Liu. “Image super-resolution via deep recursive residual network”. In: *Proceedings of the IEEE conference on computer vision and pattern recognition*. 2017, pp. 3147–3155.
- [43] Min Ji et al. “A Comparative Study of Texture and Convolutional Neural Network Features for Detecting Collapsed Buildings After Earthquakes Using Pre- and Post-Event Satellite Imagery”. In: *Remote Sensing* 11.10 (2019), p. 1202.
- [44] David G Lowe. “Distinctive image features from scale-invariant keypoints”. In: *International journal of computer vision* 60.2 (2004), pp. 91–110.
- [45] Shaoqing Ren et al. “Faster r-cnn: Towards real-time object detection with region proposal networks”. In: *Advances in neural information processing systems*. 2015, pp. 91–99.
- [46] Tsung-Yi Lin et al. “Feature pyramid networks for object detection”. In: *Proceedings of the IEEE Conference on Computer Vision and Pattern Recognition*. 2017, pp. 2117–2125.
- [47] Bryan C Russell et al. “LabelMe: a database and web-based tool for image annotation”. In: *International journal of computer vision* 77.1-3 (2008), pp. 157–173.
- [48] Satoshi Suzuki et al. “Topological structural analysis of digitized binary images by border following”. In: *Computer vision, graphics, and image processing* 30.1 (1985), pp. 32–46.
- [49] Berthold KP Horn. “Hill shading and the reflectance map”. In: *Proceedings of the IEEE* 69.1 (1981), pp. 14–47.
- [50] Sergey Ioffe and Christian Szegedy. “Batch normalization: Accelerating deep network training by reducing internal covariate shift”. In: *arXiv preprint arXiv:1502.03167* (2015).
- [51] Andrew W Fitzgibbon, Robert B Fisher, et al. *A buyer’s guide to conic fitting*. University of Edinburgh, Department of Artificial Intelligence, 1996.
- [52] TY Zhang and Ching Y Suen. “A fast parallel algorithm for thinning digital patterns”. In: *Communications of the ACM* 27.3 (1984), pp. 236–239.